

Achiral dielectric metasurfaces for spectral and polarization control of valley specific light emission from monolayer MoS₂

Yin Liu*^{1†}, Sze Cheung Lau^{*2}, Wen-Hui Sophia Cheng^{1,3}, Amalya Johnson¹, Qitong Li¹, Emma Simmerman², Ouri Karni^{2,5}, Jack Hu¹, Fang Liu³, Mark L. Brongersma¹, Tony F. Heinz^{2,5} and Jennifer A. Dionne¹

¹Department of Materials Science and Engineering, Stanford University, Stanford, CA 94305, USA

²Department of Applied Physics, Stanford University, Stanford, CA 94305, USA

³Department of Materials Science and Engineering, National Cheng Kung University, Tainan 701, Taiwan

⁴Department of Chemistry, Stanford University, Stanford, CA 94305, USA

⁵SLAC National Accelerator Laboratory, 2575 Sand Hill Road Menlo Park, CA 94025

† Present address: Department of Materials Science and Engineering, North Carolina State University

* These authors contributed equally to this work

Corresponding authors: Yin Liu (yliu292@ncsu.edu) and Jennifer Dionne(jdionne@stanford.edu)

Abstract:

Two-dimensional transition metal dichalcogenides host robust excitons with a valley degree of freedom that can be optically accessed and manipulated for quantum information processing. Here, we demonstrate enhancement and spectral control of valley exciton emission in MoS₂ via coupling with dielectric metasurfaces composed of arrays of Si nano-disks. By varying the disk diameter, we tune the frequencies of Mie scattering modes of the disks to match the exciton frequency in MoS₂. Photoluminescence (PL) intensity of MoS₂ is enhanced by over 30 times on the metasurface in contrast to that on flat sapphire substrate, attributed to enhancement of both excitation and emission resulting from the metasurface optical near field coupling. The MoS₂ emission spectra are also markedly modified via the coupling of neutral excitons, trions and defect bound excitonic states with the metasurface Mie modes. Finally, we show how the metasurface enhances the valley polarized PL from both excitons and trions by over an order of magnitude at cryogenic temperatures (100K). The observed disk-diameter dependent enhancement shows excellent agreement with the calculated Purcell factor of our metasurfaces. Our study provides a Si-compatible photonic design to improve the recombination dynamics of valley polarized excitons and trions for a variety of on-chip valleytronic applications.

Introduction

In two-dimensional transition metal dichalcogenides (TMDCs), carriers and excitons at different K and K' valleys carry different pseudospins. The pseudospin-valley coupling gives rise to a valley degree of freedom which holds great promise for quantum information processing and storage¹⁻⁴. Valley-specific excitonic states in these materials can be coupled to chiral photon states through angular momentum transfer and therefore the readout and control of the valley states can be achieved using circularly polarized light (CPL) with different helicity. The exciton-photon interaction also enables the use of the valley states for chiral and quantum light emitting devices⁵. Achieving valley-selective exciton populations and radiation is the key to exploiting the valley degree of freedom. Valley-selective photoluminescence (PL) can be observed and quantified by the degree of polarization (DOP), defined as $DOP = [I(\sigma+) - I(\sigma-)]/[I(\sigma+) + I(\sigma-)]$, where $I(\sigma+/-)$ are right and left circularly polarized PL intensities. However, the magnitude of DOP is limited by the decoherence processes such as the intervalley scattering. The decrease of valley polarization at elevated temperatures limits room-temperature application of valleytronics.

TMDCs have been integrated with plasmonic nanostructures and metasurfaces and resonant light-exciton coupling in these hybrid platforms enhances the valleytronic properties in many aspects. For instance, plasmonic nanowire waveguides and metasurfaces have been used to enhance and direct the chiral emission from excitons at different valleys to different directions and the spatial separation of emission is desirable for the readout of valley information⁶⁻¹⁰. On the other hand, chiral metasurfaces and nanostructures have been used to enhance valley polarization of photoluminescence and significant valley polarization can be retained at room temperature¹¹⁻¹⁵. The enhancement primarily results from enhanced chiral field of the metasurface that enhances the radiative decay of chiral photon states, known as chiral Purcell effect^{11,16}. However, these chiral metasurfaces suffer from three main drawbacks limiting their applications for valleytronics: 1) the effect of the chiral metasurfaces on the radiative recombination at the two different valleys is opposite. The valley polarization is enhanced when helicity of the excitation light matches the chirality of the metasurface, whereas it is suppressed if helicity of excitation is switched. 2) the resonance of chiral structures can notably change the polarization of the excitation field, generating excitons at both valleys even if incidence light is purely circularly polarized and 3) the chiral metasurfaces can notably modify the circular polarization of valley-specific emissions, greatly complicating the readout of valley information via DOP measurement.

In this work, we address these challenges by integrating exfoliated MoS₂ monolayers with an achiral dielectric metasurfaces comprised of Si disk arrays (Fig. 1a). The achiral disks are designed to preserve the handedness of the incident light source, with a uniform-sign local density of chirality (C). By varying the disk diameter, we find that the emission spectral shape of MoS₂ neutral excitons, trions or defect bound excitonic states can be modified and dominated by the radiative Mie modes of the metasurfaces. We also show that our achiral metasurfaces exhibit equal enhancement of valley polarized PL under CPL excitation with different helicities, in stark-contrast with previous studies^{11,13}. The measured DOP shows a dependence on the metasurface disk resonances that is consistent with the radiative decay enhancement and Purcell factor enabled by the metasurfaces (Fig. 1b).

Si nanodisk arrays were fabricated in single-crystalline silicon layers on sapphire substrates (silicon on sapphire chips) via e-beam lithography patterning of hydrogen silsesquioxane (HSQ) resist and dry etching (see Methods in SI). Three sets of metasurfaces were fabricated on three silicon on sapphire chips with

different thickness, two with disk height $h= 100$ nm and one with $h= 96$ nm respectively. Each set contains 12-15 metasurfaces, where each metasurface has a different disk diameter ranging from 210 to 285 nm. All metasurfaces have an array area of 100 μm by 100 μm and a fixed pitch of 350 nm. The metasurfaces with $h=100$ nm were used for non-polarization resolved measurements and the metasurfaces with $h=96$ were used for polarization resolved measurements. Figure 2a shows the top-down SEM images of three nanodisk arrays with varying diameters. Cross-sectional SEM imaging (Fig.2b) confirms the disk geometry with a sharp side wall.

We simulated the transmission spectra of the metasurfaces with $h= 100$ nm and $d=220-290$ nm using finite difference time domain simulations (Fig.2c). Two dips can be identified in the spectra, corresponding to electric dipole (ED) and magnetic dipole (MD) Mie resonances respectively. We confirm the dipolar nature of the two modes by plotting the magnitude and direction of the electric field, denoted by the colormaps and the arrows in Figure 2d , respectively. As we change the aspect ratio of the disks by varying the diameter, the resonant frequencies shift. With decreasing aspect ratio, both resonances shift to shorter wavelengths, while the electric dipolar mode shifts more than the magnetic dipolar mode, and the two dips begin to overlap. At a diameter of 240 nm, the two modes overlap at 660 nm which is close to A-exciton energy of MoS_2 at room temperature. The closely spaced modes also lead to an increased transmission, indicating a first Kerker-like condition is reached ¹⁷⁻¹⁹. At this condition, the local density of chirality is enhanced and allows preservation of the incident-light polarization state (S.I. Fig. 1).^{17,18,20} The measured transmission of our fabricated metasurfaces show excellent agreement with simulated results (Fig. 2e).

MoS_2 monolayers were exfoliated from bulk single crystals using the gold tape method, yielding high-quality single crystal monolayers with a lateral size of a few millimeters.²¹ The monolayers were then transferred onto the silicon disk arrays (see Methods in SI). Significant benefit can be derived from using such large-scale exfoliated samples, which enables the coverage of almost full-sets of metasurfaces on a single chip by the same monolayer crystal and therefore allows comparison of the results from different metasurfaces. Figure 2f shows a photo of MoS_2 on a set of metasurfaces with $h=100$ nm. Most areas of the metasurfaces are covered by the MoS_2 single layer after the transfer. No significant strain is expected in the layer after the transfer except at the edge of the pattern, due to the relatively low aspect ratio of the disks and high filling ratio of the patterns. This is confirmed by our SEM imaging, showing a flat and smooth layer with little corrugation on top of the metasurfaces (Fig. 2g). Figure 2h shows representative Raman spectra collected from MoS_2 on metasurface with $d= 245$ nm and on sapphire around metasurface. The Raman peaks at 386 cm^{-1} and 404 cm^{-1} in the spectrum collected from MoS_2 on sapphire are attributed to E_{2g}^1 and A_{1g} phonon modes respectively, and the 18 cm^{-1} frequency separation between these two modes confirms the single layer nature of the specimen ²². On the metasurface, E_{2g}^1 mode shifts to 385 cm^{-1} whereas A_{1g} mode stays the same. The redshift may result from moderate tensile strain in the MoS_2 due to the transfer process or from the modification of electron-phonon coupling by silicon metasurfaces. The Raman intensity is also enhanced by ~ 10 times on the metasurface, resulting from the enhanced excitation field at 532 nm with the presence of metasurfaces.

The coupling of the MoS_2 monolayer with the metasurface is in the weak coupling regime. We simulated the transmission spectra of the monolayer on the metasurface with dielectric constant of MoS_2 retrieved from a prior study (S.I. Fig.2a)²³. The transmission spectra are still dominated by the overlapped ED and MD modes of metasurfaces in the presence of MoS_2 , whereas transmission slightly decreases and the

transmission dip shows blueshift of 2 nm (S.I. Fig.2b). There is no signature of anti-crossing behavior or Rabbi splitting where exciton and Mie modes would have strong coupling to form mixed polaritonic states^{24,25}.

The coupling of the MoS₂ with metasurfaces was examined using photoluminescence spectroscopy. Figure 3a shows the PL spectra of MoS₂ on silicon arrays with varying diameters d under 532 nm excitation at room temperature. With d increasing from 240 nm to 285 nm, the PL spectral shape changes significantly with an increasing number (1-3) of emission peaks, resulting from the coupling of excitons with radiative metasurface modes. To make the correlation, we deconvolute the PL spectra using three Lorentzian functions representing the ED mode, A-exciton mode and MD modes (S.I. Fig 3). For metasurfaces with modes overlapping or closely spaced in the spectra, one or two Lorentzian functions were used for the fit, assuming that the metasurface modes dominate the emission peak in contrast to the exciton. The mode wavelengths extracted from fitting the PL spectra are shown in Figure 3b, which shows a very good correspondence with positions of dips resulting from ED and MD modes in transmission spectra (Fig. 1e) of the bare metasurfaces without MoS₂. Note that the metasurface with d=280 nm was not covered by MoS₂ after the transfer and only data from the transmission spectrum is shown.

We also cooled the sample down to 5 K and measured the PL spectra (Fig. 3c). PL peak of neutral A excitons shifts from 665 nm at room temperature to 624 nm at 5K, corresponding to an increased A-exciton energy at lower temperatures. A broad defect emission band denoted as the L band, resulting from defect bound excitonic states, is present and dominates the emission spectra at 5K. At cryogenic temperatures, the strain generated by depositing TMDCs on nanopillars could have localized excitons, giving rise to single photon emission with narrow emission linewidth.^{26,27} Such emission was not observed in our samples, consistent with a low strain in the MoS₂ deposited on high-filling-ratio metasurfaces. The defect bound states are coupled to the Mie modes which enhances their emission intensities. The emission peak redshifts from 665 to 696 nm with increasing disk diameters, in correspondence to the redshift of the ED and MD modes in the metasurfaces. The results suggest the strong capability of using radiative Mie modes of dielectric metasurface for the spectral control of various excitonic emissions from 2D materials.

The PL intensity of MoS₂ is significantly enhanced by 30 times on the metasurface with d=245nm in contrast to flat sapphire substrate at room temperature (Fig.1d). The enhancement is clear in the corresponding intensity map, showing a small variation in intensity on the metasurface(Fig.1e) and suggesting that the monolayer has uniform optical properties. The enhancement is attributed to enhancement in both absorption and emission resulting from the optical near field around the metasurfaces. We performed simulation and calculated the absorption of MoS₂ on metasurfaces and on sapphire substrate respectively and the result suggests ~3 times enhancement of absorption on the metasurface under 532 nm excitation (S.I. Fig 4) The result is also consistent with the measured 10 times enhancement in the Raman intensity on the metasurface(Fig. 1j) since $I_{Raman} \propto |E_{exc}|^4$ (whereas $I_{abs} \propto |E_{exc}|^2$) . Our analysis therefore suggests a 10 times emission enhancement resulting from enhanced near field and Purcell effect on the radiative decay of excitons.

To verify the Purcell effect, we transferred a MoS₂ monolayer encapsulated with a few nanometer thick hBN on both sizes onto a metasurface and performed time-resolved PL measurement using a 485 nm pulsed laser with a 60 ps pulse width and a repetition frequency of 80 MHz (see Methods in SI). Figure 2f shows

the normalized luminescence intensity dynamics of the neutral excitons of MoS₂ monolayers on sapphire and on metasurface respectively at room temperature. The kinetics can be fitted well using a Gaussian response function convoluted with a biexponential decay function of $Ae^{-t/\tau_1} + Be^{-t/\tau_2}$. Two distinct time constants in the biexponential function are extracted, giving rise to a fast decay (τ_1) of 0.2–0.32 ns and slow decay (τ_2) of 0.94–3 ns. The fast decay and slow decay are attributed to the recombination of neutral free excitons and recombination of defect trapped or phonon scattered excitons respectively²⁸. The overall decay time of excitons on the metasurface is shortened from 0.32 ns on the sapphire to 0.2 ns on the metasurface.

The decay time is determined by both radiative and nonradiative recombination processes via $\frac{1}{\tau_1} = \frac{1}{\tau_r} + \frac{1}{\tau_{nr}}$. The overall decay time is decreased by the significant reduction of radiative recombination time resulting from the Purcell effect of the metasurface. Note that at room temperature the recombination is dominated by the nonradiative recombination. With the hBN encapsulation, we assume nonradiative decay time is the same for the monolayer on sapphire and metasurface. Taking an estimation of $\tau_r = 10 \tau_{nr}$, we estimate that the radiative recombination time τ_r on metasurface decreases to be 13% of τ_r on sapphire. Our time-resolved PL results in combination with the PL enhancement suggests a significant enhancement of radiative recombination rate due to the near field of the metasurfaces.

Next, we studied the tailoring of polarization of emission from valley excitons by the metasurfaces through valley-resolved PL measurement. In our measurements, 633 nm and 610 nm circularly polarized laser excitations are used to create exciton at specific valleys and the circular polarization state of emitted photons is analyzed by the degree of polarization (DOP), defined as $DOP = [I(\sigma+) - I(\sigma-)]/[I(\sigma+) + I(\sigma-)]$, where $I(\sigma+/-)$ are right and left circularly polarized PL intensities. A schematic of the setup for the valley resolved measurement is shown in S.I. Figure 5. The DOP is determined by the initial polarization P_0 , exciton

lifetime τ and valley depolarization time τ_s via $DOP = \frac{P_0}{1 + \tau/\tau_s}$. At higher temperatures, valley depolarization time is decreased due to increasing intervalley scattering. We could not detect any DOP from our samples at temperatures above 200K. The measurements were thus performed at 100 K where significant DOP can be detected. Figure 4 and S.I. figure 6 show the CPL resolved PL spectra and DOP spectra of MoS₂ on metasurfaces with varying disk diameters and $h=96$ nm using 610 nm circularly polarized excitation. Two peaks at 630 nm and 642 nm can be clearly resolved in the spectra, which are attributed to emission from neutral excitons and trions respectively. Under excitation of CPL with different helicities, the spectral shapes and intensities are almost the same except the flip of polarization sign, giving rise to symmetric DOPs for different excitation helicities. This demonstrates the achiral property of our metasurfaces, in stark contrast to the asymmetric DOP results on TMDCs on chiral nanophotonic structures reported in previous studies^{11,13}.

We plot DOPs measured at the emission wavelength of excitons (630 nm) and trion emissions (642 nm) for different metasurfaces, showing a clear dependence of DOPs on the disk diameters (Fig.5). The DOPs of excitons and trions show a maximum of 24% at $d = 220$ and 9 % at $d = 230$ nm respectively, and both drop to zero with d deviating from these values. In addition to the 610 nm excitation, we also measured CPL resolved PL using 633 nm excitation. In this case, the PL of excitons is cut off at 639 nm by a long pass filter and only DOP of trions at 642 nm was measured (S.I. Fig 7). The resonant coupling of 633 nm laser with excitons leads to significantly higher PL intensity and larger DOP overall (S.I. Fig 8 and S.I. Fig 9).

Figure 5 also plots the dependence of trion DOP on the disk diameters, showing a maximum value to be 34% at $d=220\text{-}230\text{ nm}$. The trend is very similar to the trend obtained from 610 nm excitation.

Our results show that the valley polarization of excitonic states can be significantly affected by the near field associated with Mie modes of metasurfaces. The maximum DOPs were observed on metasurface with closely-spaced MD and ED modes, resulting in a strong enhancement in the near field. To illustrate this, we calculated the radiative enhancement of MoS_2 on metasurfaces using COMSOL. The room-temperature dielectric function of silicon was used in the simulation. This is justified by our measured reflection spectra of bare metasurfaces at room temperature and 100K, showing little change in the spectra shape governed by Mie resonances of the nanodisks (S.I. Fig 10). To represent the valley excitons, we use a cloud of in-plane chiral dipoles formed by pairs of two orthogonal electric dipoles with a phase difference of 90 degrees. 100 chiral dipoles are placed in random orientation and phases on the surface above the nanodisk in a unit cell. The Purcell Factor F_p of the metasurface is calculated by dividing emitted power with the presence of metasurface by the emitted power without metasurface. The dependence of F on disk diameters at the peak wavelength for trion (642nm) and exciton (630 nm) is shown in Figure 5, showing a very good agreement with the dependence of the measured DOP. In the plot, d corresponding to the maximum of F_p shifts to smaller values at decreased wavelength, which is also consistent with the shift of d associated maximum DOP for trion and excitons . The modulation of DOP can be well correlated to the enhancement of radiative recombination on the metasurfaces. The modulation of DOP by our metasurface is achieved at cryogenic temperatures (100K), where Purcell enhanced radiative recombination is comparable with the non-radiative recombination. Further implementation at elevated temperatures requires metasurfaces and resonators with improved designs. For instance, the recently designed high-quality-factor dielectric metasurface that enables Purcell enhancement two orders of magnitude larger than that of current metasurface is promising for future studies²⁹⁻³¹.

In summary, we integrated exfoliated MoS_2 monolayers with achiral silicon nanodisk metasurfaces and studied the effect of Mie resonances and near optical field on the excitonic emissions. We show that the emission spectral shape of MoS_2 can be markedly modified via the coupling of neutral excitons, trions or defect bound excitonic states with the metasurfaces, with emission peaks governed by radiative Mie modes of metasurfaces. Most importantly, using an achiralstructures, we identify the role of Purcell effect of metasurfaces in affecting the valley exciton recombination and relaxation dynamics via our valley resolved PL measurements. Our work provides a key understanding about the exciton-photon coupling for future application of TMDC based valleytronic devices.

Author information

Y. L. and S.C.L. contributed equally to this work.

Acknowledgements

The authors acknowledge support from the Photonics at Thermodynamic Limits Energy Frontier Research Center, funded by the U.S. Department of Energy, Office of Science, Office of Basic Energy Sciences, under award no. DE-SC0019140, which supported the salaries of Y. L, K. S, M. B. and J. D. In addition, the authors acknowledge support for quantum materials synthesis, fabrication, and characterization from the Q-next grant under award no. DE-AC02-76SF00515. T. H. salary was supported by the Moore Foundation grant under award no. 10146. W.-H.C. acknowledges the support from Ministry of Science and Technology, Taiwan (2030 Cross-Generation Young Scholars Program, MOST 110-2628-E-006-007), and Ministry of Education (Yushan Fellow Program), Taiwan, and in part from the Higher Education Sprout Project of the Ministry of Education to the Headquarters of University Advancement at National Cheng Kung University (NCKU). The authors thank Dr. Yongmin Liu in Northeastern University for valuable input into the work.

References

1. Mak, K. F., He, K., Shan, J. & Heinz, T. F. Control of valley polarization in monolayer MoS₂ by optical helicity. *Nat. Nanotechnol.* **7**, 494–498 (2012).
2. Zeng, H., Dai, J., Yao, W., Xiao, D. & Cui, X. Valley polarization in MoS₂ monolayers by optical pumping. *Nat. Nanotechnol.* **7**, 490–493 (2012).
3. Xu, X., Yao, W., Xiao, D. & Heinz, T. F. Spin and pseudospins in layered transition metal dichalcogenides. *Nat. Phys.* **10**, 343–350 (2014).
4. Wang, G. *et al.* *Colloquium* : Excitons in atomically thin transition metal dichalcogenides. *Reviews of Modern Physics* vol. 90 Preprint at <https://doi.org/10.1103/revmodphys.90.021001> (2018).
5. Schaibley, J. R. *et al.* Valleytronics in 2D materials. *Nature Reviews Materials* **1**, 1–15 (2016).
6. Gong, S.-H., Alpeggiani, F., Sciacca, B., Garnett, E. C. & Kuipers, L. Nanoscale chiral valley-photon interface through optical spin-orbit coupling. *Science* **359**, 443–447 (2018).
7. Sun, L. *et al.* Separation of valley excitons in a MoS₂ monolayer using a subwavelength asymmetric groove array. *Nat. Photonics* **13**, 180–184 (2019).
8. Hu, G. *et al.* Coherent steering of nonlinear chiral valley photons with a synthetic Au–WS₂

metasurface. *Nat. Photonics* **13**, 467–472 (2019).

- 9. Bucher, T. *et al.* Tailoring Photoluminescence from MoS₂ Monolayers by Mie-Resonant Metasurfaces. *ACS Photonics* **6**, 1002–1009 (2019).
- 10. Cihan, A. F., Curto, A. G., Raza, S., Kik, P. G. & Brongersma, M. L. Silicon Mie resonators for highly directional light emission from monolayer MoS₂. *Nat. Photonics* **12**, 284–290 (2018).
- 11. Li, Z. *et al.* Tailoring MoS₂ valley-polarized photoluminescence with super chiral near-field. *Adv. Mater.* **30**, e1801908 (2018).
- 12. Lin, W.-H. *et al.* Electrically tunable and dramatically enhanced valley-polarized emission of monolayer WS₂ at room temperature with plasmonic Archimedes spiral nanostructures. *Adv. Mater.* **34**, e2104863 (2022).
- 13. Wen, T. *et al.* Steering valley-polarized emission of monolayer MoS₂ sandwiched in plasmonic antennas. *Science Advances* vol. 6 Preprint at <https://doi.org/10.1126/sciadv.aa00019> (2020).
- 14. Wu, Z., Li, J., Zhang, X., Redwing, J. M. & Zheng, Y. Room-temperature active modulation of valley dynamics in a monolayer semiconductor through chiral Purcell effects. *Adv. Mater.* **31**, e1904132 (2019).
- 15. Guddala, Bushati, Li & Khanikaev. Valley selective optical control of excitons in 2D semiconductors using a chiral metasurface. *Opt. Mater.* .
- 16. Yoo, S. & Park, Q.-H. Chiral Light-Matter Interaction in Optical Resonators. *Phys. Rev. Lett.* **114**, 203003 (2015).
- 17. Solomon, M. L., Hu, J., Lawrence, M., García-Etxarri, A. & Dionne, J. A. Enantiospecific Optical Enhancement of Chiral Sensing and Separation with Dielectric Metasurfaces. *ACS Photonics* **6**, 43–49 (2019).
- 18. Abendroth, J. M. *et al.* Helicity-preserving metasurfaces for magneto-optical enhancement in ferromagnetic [pt/co] N films. *Adv. Opt. Mater.* **8**, 2001420 (2020).
- 19. Staude, I. *et al.* Tailoring directional scattering through magnetic and electric resonances in subwavelength silicon nanodisks. *ACS Nano* **7**, 7824–7832 (2013).

20. Solomon, M. L., Abendroth, J. M., Poulikakos, L. V., Hu, J. & Dionne, J. A. Fluorescence-Detected Circular Dichroism of a Chiral Molecular Monolayer with Dielectric Metasurfaces. *J. Am. Chem. Soc.* **142**, 18304–18309 (2020).

21. Liu, F. *et al.* Disassembling 2D van der Waals crystals into macroscopic monolayers and reassembling into artificial lattices. *Science* **367**, 903–906 (2020).

22. Li, H. *et al.* From bulk to monolayer MoS₂: Evolution of Raman scattering. *Adv. Funct. Mater.* **22**, 1385–1390 (2012).

23. Li, Y. *et al.* Measurement of the optical dielectric function of monolayer transition-metal dichalcogenides: MoS₂, MoSe₂, WS₂, and WSe₂. *Phys. Rev. B Condens. Matter Mater. Phys.* **90**, (2014).

24. Liu, X. *et al.* Strong light–matter coupling in two-dimensional atomic crystals. *Nat. Photonics* **9**, 30–34 (2014).

25. Chen, Y.-J., Cain, J. D., Stanev, T. K., Dravid, V. P. & Stern, N. P. Valley-polarized exciton–polaritons in a monolayer semiconductor. *Nat. Photonics* **11**, 431–435 (2017).

26. Branny, A., Kumar, S., Proux, R. & Gerardot, B. D. Deterministic strain-induced arrays of quantum emitters in a two-dimensional semiconductor. *Nat. Commun.* **8**, 15053 (2017).

27. Palacios-Berraquero, C. *et al.* Large-scale quantum-emitter arrays in atomically thin semiconductors. *Nat. Commun.* **8**, 15093 (2017).

28. Korn, T., Heydrich, S., Hirmer, M., Schmutzler, J. & Schüller, C. Low-temperature photocarrier dynamics in monolayer MoS₂. *Appl. Phys. Lett.* **99**, 102109 (2011).

29. Hu, J., Lawrence, M. & Dionne, J. A. High Quality Factor Dielectric Metasurfaces for Ultraviolet Circular Dichroism Spectroscopy. *ACS Photonics* **7**, 36–42 (2020).

30. Lawrence, M. *et al.* High quality factor phase gradient metasurfaces. *Nat. Nanotechnol.* **15**, 956–961 (2020).

31. Lawrence, M. & Dionne, J. A. Nanoscale nonreciprocity via photon-spin-polarized stimulated Raman scattering. *Nat. Commun.* **10**, 3297 (2019).

Main figures

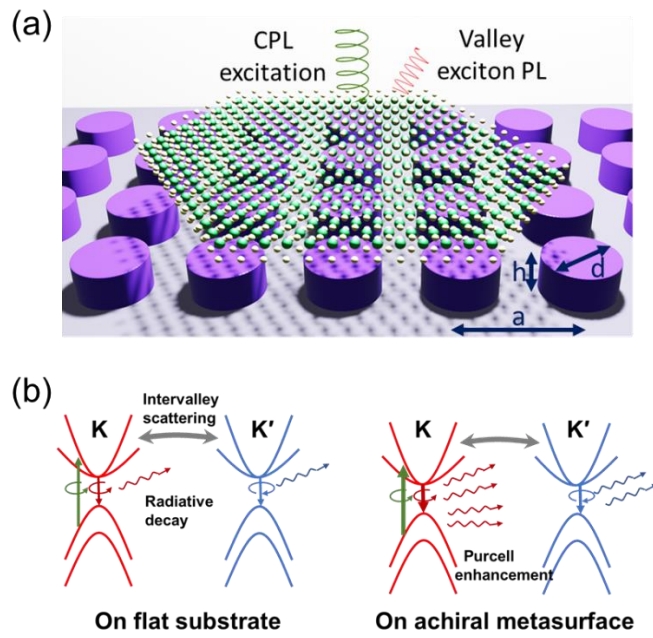


Figure 1 Coupling monolayer MoS_2 with achiral dielectric metasurface for enhancing valleytronic properties of TMDCs. (a) Schematic showing the interfacing of a single layer TMDCs with a Si metasurface. (b) Schematic showing the excitation and decaying of valley excitons with significant intervalley scattering (Left) and enhanced radiative decay of valley excitons resulting from chiral Purcell effect of the dielectric metasurface (Right).

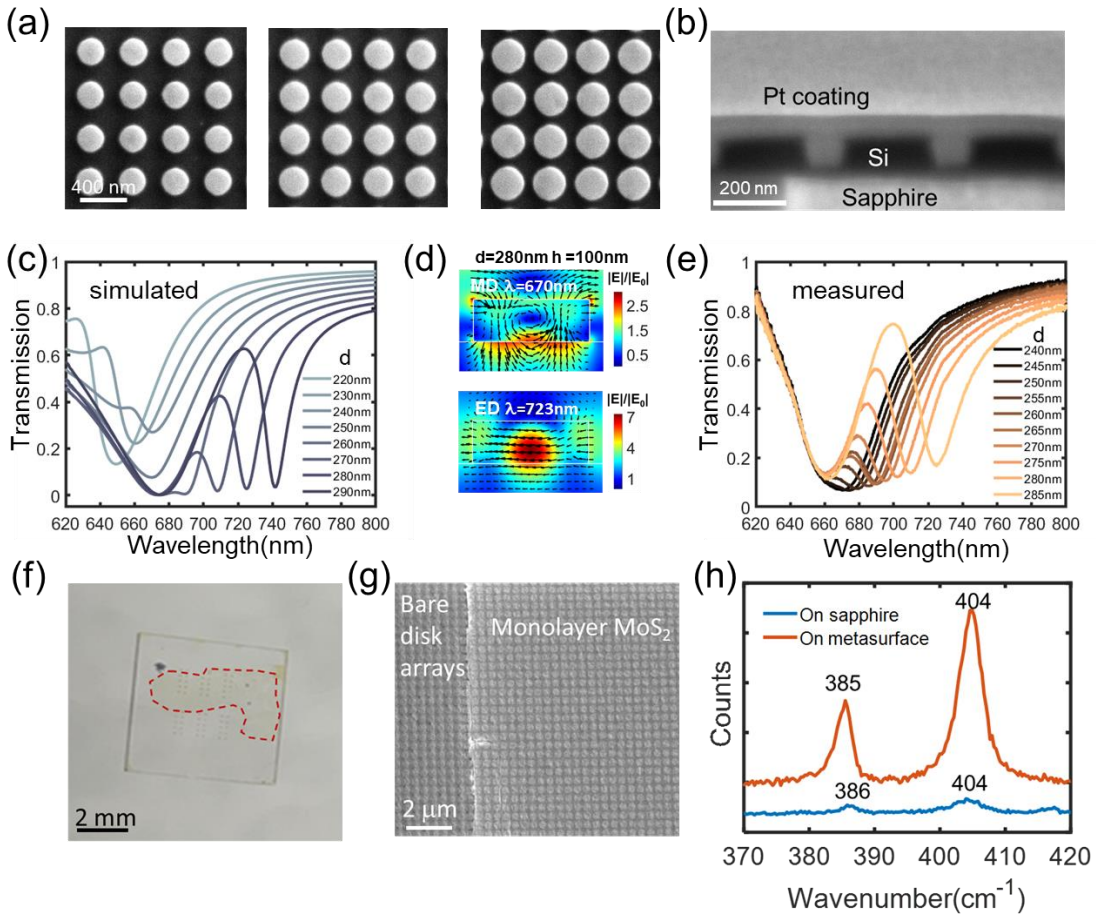


Figure 2 (a) Top-down and (b) Cross-sectional SEM images of Si disk arrays. (c) Simulated transmission spectra of Si dielectric arrays with $h = 100$ nm and radius 210–290 nm, where the dips result from electric dipole and magnetic dipole resonances. (d) Electric field intensity and vector map of the ED and MD mode. (e) Measured transmission spectra of Si disk arrays with varying diameters. (f,g) Optical photo and SEM image showing a large-scale single layer MoS₂ transferred on metasurfaces. The monolayer MoS₂ flake is highlighted by red dashed line (h) Raman spectra of single-layer MoS₂ on metasurface and sapphire respectively.

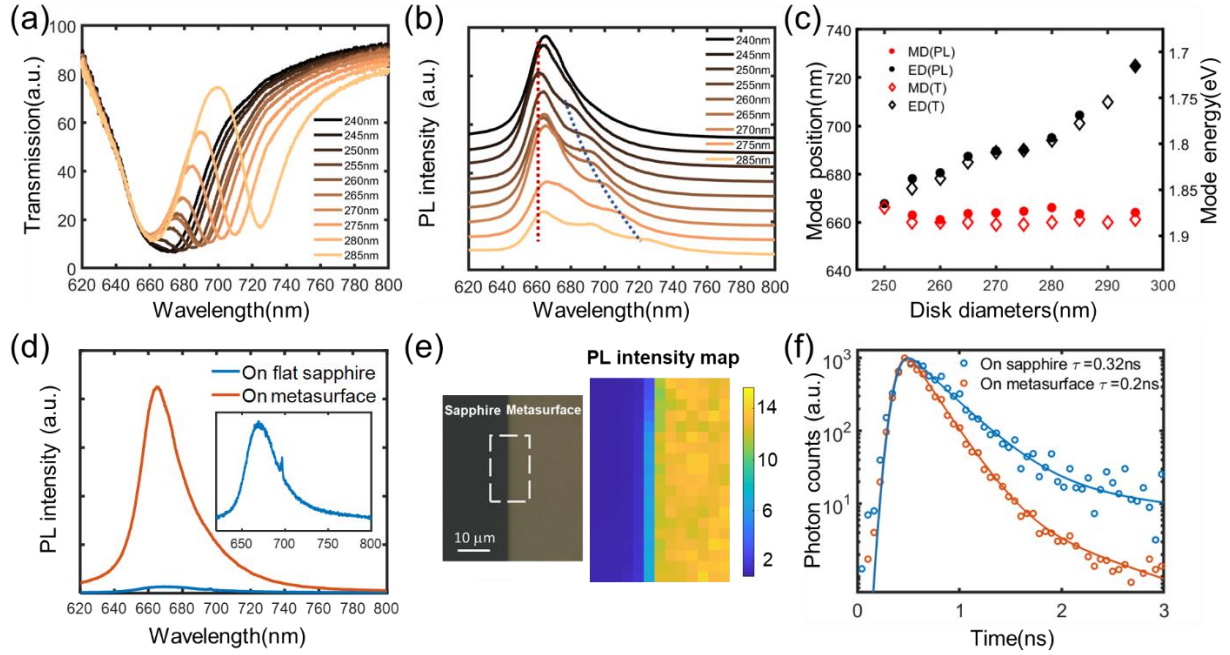


Figure 3 Modulation of PL spectral shapes and intensity of excitonic emission by metasurfaces (a) PL of MoS₂ on metasurfaces with varying diameters at 5K. (b) Fitted energy of radiative metasurface modes versus disk diameters. (c) Normalized PL spectra of MoS₂ on metasurfaces with varying disk diameters at 5K. (d) Photoluminescence spectra of MoS₂ on metasurface (red) and flat sapphire (blue) at 5K. Inset: PL of MoS₂ on sapphire. (e) Optical image showing MoS₂ covering both metasurface and sapphire (left) and the corresponding PL intensity map (right). The map area is marked by the dashed box in the optical image. (f) Time resolved PL of an encapsulated MoS₂ on metasurface and flat sapphire.

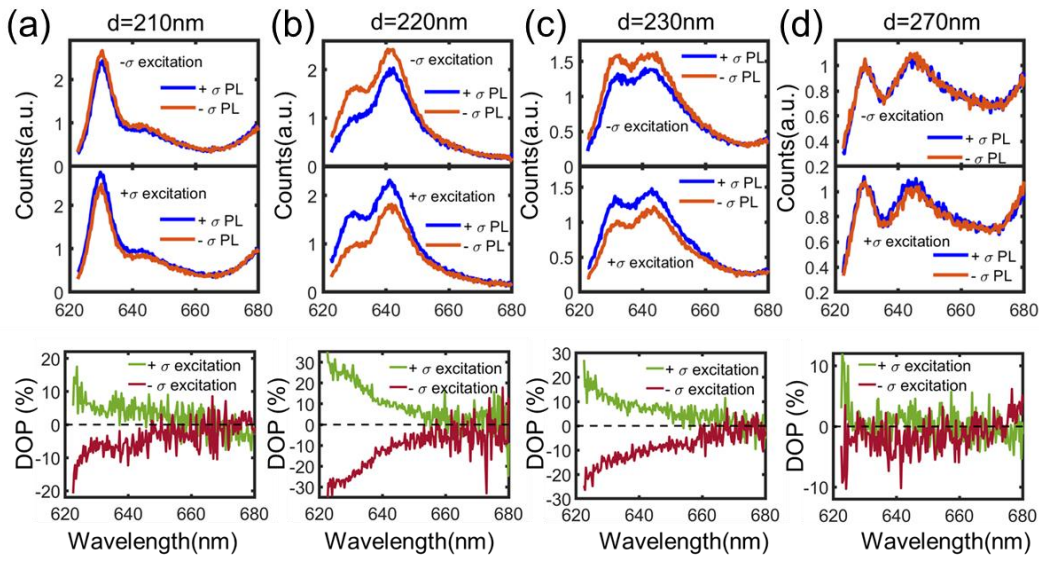


Figure 4 **Valley-resolved PL of excitons and trions under 610 nm excitation** (a-d) detected circular polarized PL (upper panel) and degree of polarization (lower panel) under left-handed and right-handed circularly polarized laser excitation respectively for MoS₂ on a metasurface with $d = 210, 220, 230$ and 270nm .

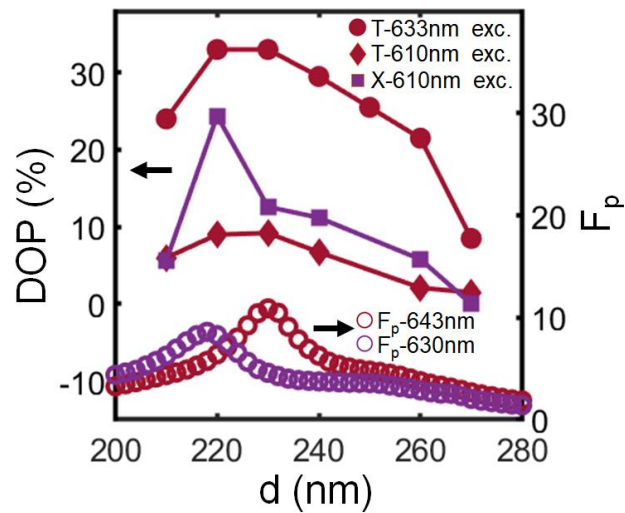


Figure 5 Measured trion and exciton DOP excited with 610 nm and 633 nm lasers and calculated Purcell enhancement versus disk diameter d .